Geophysical Research Letters

RESEARCH LETTER
10.1029/2025GL121533

Key Points:

- We use a three-dimensional global hybrid simulation to study magneto-sheath jets formed by shock–discontinuity interactions (SDIs) and the magnetopause responses
- SDIs deform bow shock, redirect flows with little slowdown, and expansion of hot flow anomaly compresses flanks to form ribbon-like jets
- The jets span the entire dayside magnetosheath and reach ~40 R_E along the discontinuity downstream of both quasi-parallel and quasi-perpendicular shocks

Supporting Information:

Supporting Information may be found in the online version of this article.

Correspondence to:

S. Lu and Q. Lu,
lusan@ustc.edu.cn;
qmlu@ustc.edu.cn

Citation:

Guo, J., Lu, S., Lu, Q., Zhou, Y., Wang, B., Sun, T., et al. (2026). Large-scale magnetosheath jets formed by shock-discontinuity interactions: A three-dimensional global hybrid simulation. *Geophysical Research Letters*, *53*, e2025GL121533. https://doi.org/10.1029/2025GL121533

Received 25 DEC 2025
Accepted 17 APR 2026

Large-Scale Magnetosheath Jets Formed by Shock-Discontinuity Interactions: A Three-Dimensional Global Hybrid Simulation

Jin Guo[1], San Lu[1], Quanming Lu[1], Yufei Zhou[2], Boyi Wang[3], Tianran Sun[4], Yihong Guo[5], Zhongwei Yang[4], Shimou Wang[1], Junyi Ren[1], Jiuqi Ma[1], Chao Shen[2], Xinliang Gao[1], and Rongsheng Wang[1]

[1]National Key Laboratory of Deep Space Exploration/School of Earth and Space Sciences, University of Science and Technology of China, Hefei, China, [2]School of Science, Harbin Institute of Technology (Shenzhen), Shenzhen, China, [3]School of Aerospace Science, Harbin Institute of Technology (Shenzhen), Shenzhen, China, [4]State Key Laboratory of Solar Activity and Space Weather, National Space Science Center, Chinese Academy of Sciences, Beijing, China, [5]Aerospace Information Research Institute, Chinese Academy of Sciences, Beijing, China

Abstract Magnetosheath high-speed jets with enhanced dynamic pressure are common in Earth's magnetosheath and can impinge on the magnetopause, driving pronounced boundary deformation. Recent observations indicate that shock–discontinuity interactions (SDIs) can generate magnetosheath jets, but the formation mechanism is still unclear. Using a three-dimensional global hybrid simulation, we investigate SDI-driven magnetosheath jets. SDI-driven deformation of the bow shock redirects the solar wind according to the Rankine–Hugoniot relations—deflecting the flow along the shock with little deceleration—thereby producing ribbon-like jets flanking the core of a hot flow anomaly. The jets span the entire dayside magnetosheath and reach ~40 Earth radii (R_E) along the discontinuity downstream of both quasi-parallel and quasi-perpendicular shocks. The SDI-driven structures produce a magnetopause distortion that attains an amplitude of ~5 R_E and extends ~17 R_E along the discontinuity, propagating from the dayside to the nightside. Synthetic soft X-ray images derived from the simulation indicate that SDI-driven structures should be detectable by forthcoming global soft X-ray missions.

Plain Language Summary Earth's magnetic field forms a protective bubble in the solar wind. On the Sun-facing side, a shock wave (the bow shock) stands ahead of this bubble, and the region just behind it (the magnetosheath) often contains short-lived, high-pressure "jets" of plasma that can push the boundary of the bubble (the magnetopause). Using a global computer model that includes key ion physics, we show how an abrupt change in the solar wind (a discontinuity) striking the bow shock warps it and redirects the flow rather than slowing it down. This process creates long ribbon-like jets on either side of a central hot, low-pressure cavity known as a hot flow anomaly. In our simulation, the jets span the entire dayside region, extend about 40 Earth radii, reach the magnetopause, and drive large boundary motions—bulges and dents up to about 5 Earth radii that travel with the disturbance from the dayside to the nightside. Synthetic soft X-ray images suggest these features should be detectable by future space imagers.

1. Introduction

Collisionless bow shocks form the boundary where the supersonic, super-Alfvénic solar wind encounters planetary magnetospheres, and they efficiently accelerate particles via shock-drift and diffusive shock acceleration, producing suprathermal and energetic ion and electron populations (Balogh & Treumann, 2013; Burgess et al., 2012; Guo, Lu, Lu, Yang, & Gao, 2024; Tang et al., 2025; Yang et al., 2009). A key descriptor of shock geometry is the angle θ_{Bn} between the upstream magnetic field and the local shock normal: quasi-parallel shocks ($\theta_{Bn} \lesssim 45°$) are characterized by strong upstream wave–particle interactions and extended foreshocks (Cao et al., 2009; Fu et al., 2009; Hao et al., 2021; Lu et al., 2020; Shan et al., 2020; Su et al., 2012; Wu et al., 2015; Zhang et al., 2013), whereas quasi-perpendicular shocks ($\theta_{Bn} \gtrsim 45°$) produce stronger, more abrupt compressions and deflect the flow along the shock surface (Bale et al., 2005; Krasnoselskikh et al., 2013; Lembege & Savoini, 1992; Turc et al., 2020; Yang et al., 2012).

Downstream of the bow shock, usually referred to as the magnetosheath, localized transient enhancements of dynamic pressure—magnetosheath high-speed jets—are commonly observed (Archer et al., 2012; Hietala et al., 2009; Karlsson et al., 2012; Kramer et al., 2025; Němeček et al., 1998; Plaschke et al., 2018). Magnetosheath jets typically feature increased plasma density, magnetic field, and bulk speed, with earthward flows (Archer & Horbury, 2013; Karlsson et al., 2015; Plaschke et al., 2013; Pöppelwerth et al., 2024).

They have been found in the Martian and Jovian magnetosheaths (Gunell et al., 2023; Zhou et al., 2024). It has also been suggested that they may form in the Mercury's magnetosheath and in interplanetary shock sheaths (Guo, Lu, Lu, Ren, et al., 2024; Hietala et al., 2024; Karlsson et al., 2016). At Earth, magnetosheath jets can drive bow waves inside the magnetosheath (Hietala et al., 2009; Liu et al., 2019; Ren, Lu, et al., 2024) and lead to associated particle acceleration (Raptis et al., 2025; Vuorinen et al., 2022). By impinging on and denting the magnetopause, they drive boundary motions (Escoubet et al., 2020; Němeček et al., 2023; Plaschke et al., 2016; Wang et al., 2023; Yang et al., 2024) and can trigger reconnection (Guo et al., 2026; Hietala et al., 2018), surface waves (Archer et al., 2019), and ULF fluctuations (Sun et al., 2024; Wang et al., 2018). Their effects can propagate into the magnetosphere and even the ionosphere, altering energy and mass transport (Dmitriev & Suvorova, 2015; Hietala et al., 2012; Nykyri et al., 2019), generating field-aligned currents (Ma et al., 2024), and in some cases triggering aurora (Guo et al., 2026; Han et al., 2017; Qiu et al., 2024; Wang et al., 2024). Recently, Guo et al. (2026) reported that under radial IMF conditions, a large-scale magnetopause distortion, termed a cusp-to-cusp magnetopause valley, can form. This distortion is produced when numerous jets dent the magnetopause and trigger magnetopause reconnection and associated magnetic flux transfer.

Magnetosheath jets form preferentially downstream of quasi-parallel shocks (Hietala et al., 2009; Němeček et al., 1998; Plaschke et al., 2018), and many studies suggest that smaller interplanetary magnetic field (IMF) cone angles favor jet occurrence (Guo, Lu, et al., 2022; LaMoury et al., 2021; Raptis et al., 2020; Ren et al., 2023). The majority of magnetosheath jets are thought to arise from the interactions between upstream waves and the quasi-parallel bow shock (Palmroth et al., 2018; Raptis et al., 2022; Ren et al., 2023; Suni et al., 2021). Recently, some magnetosheath jets observed downstream of quasi-perpendicular shock have been attributed to shock–discontinuity interactions (SDIs) (Zhou et al., 2023, 2024), but their formation mechanism remains poorly understood.

In this study, by employing a three-dimensional (3-D) global hybrid simulation, we show large-scale magnetosheath jets formed by SDIs and elucidate their formation mechanism. The associated magnetopause response and synthetic soft X-ray signals are also presented.

2. Simulation Model and Methods

2.1. Three-Dimensional Global Hybrid Simulation

This study uses the 3-D global hybrid code gcPIC-hybrid, which supports full-particle and hybrid simulations in general curvilinear coordinates. The framework has been applied to Earth and Mercury to study, for example, chorus excitation in a dipolar field (Lu et al., 2019), flux transfer events (Lu et al., 2022), energy conversion and plasma transport (Lu et al., 2025), and magnetosheath high-speed jets (Guo et al., 2022a, 2024b; Ren, Guo, et al., 2024). In hybrid simulations, ions are treated kinetically (as macroparticles), whereas electrons are a massless, quasi-neutral fluid; a cold, incompressible ion fluid is included to represent the plasmasphere in the inner magnetosphere. The fields are advanced self-consistently: the magnetic field via Faraday's law, the electric field from the electron momentum equation, and the electron bulk velocity from Ampère's law.

The simulation is conducted in Geocentric Solar Ecliptic (GSE) Cartesian coordinates over the domain $-24\,R_E \le x \le 32\,R_E$, $-36\,R_E \le y \le 36\,R_E$, and $-36\,R_E \le z \le 36\,R_E$. A nonuniform mesh concentrates resolution near the bow shock and magnetopause, with a minimum cell spacing of $0.06\,R_E$ and a total of $718 \times 529 \times 529$ cells. Earth's magnetic dipole is centered at the origin. Steady solar wind inflow is imposed at the boundary $x = 32\,R_E$, while the other five boundaries are set to outflow. The inner boundary, a sphere of radius $3\,R_E$ centered at the origin, is treated as perfectly conducting. The system is initialized with the dipole field confined within $x \le 10\,R_E$ and a steady solar wind for $x > 10\,R_E$. The time step is set to 2% of the ion gyroperiod in the solar wind.

Initially, the IMF is $\mathbf{B}_0 = (-3.9, 3.6, -0.6)$ nT, the solar wind velocity is $\mathbf{V}_{SW} = (-468, -11, -18)$ km/s, the number density is $N_0 = 4\ \mathrm{cm}^{-3}$, and the ion temperature is $T_{i0} = 17$ eV. The upstream ion inertial length is set to $d_{i0} = 0.05\ R_E$. Because d_{i0} is taken to be three times its typical value, simulation times are scaled by a factor of three to obtain physical times. A tangential discontinuity (TD) with an initial thickness of 0.3 R_E is injected from the upstream boundary at ~2,000 s and evolves self-consistently during its propagation. The TD convects with the solar wind and has unit normal $\boldsymbol{n} = (-0.34, -0.51, -0.79)$. Across the TD, the magnetic field changes to $\boldsymbol{B}_1 = (-4.2, -1.5, 2.7)$ nT, the number density changes to $N_1 = 3.7\ \mathrm{cm}^{-3}$, and ion temperature changes to $T_{i1} = 18$ eV.

2.2. Identification of the Magnetopause and the Bow Shock

The 3-D magnetopause is identified based on the topologies of the magnetic field lines and the pressure balance between the inside and outside of the magnetopause. For the dayside magnetopause, the position of the magnetopause is $r < 15\ R_E$. We conduct parallel calculation to trace magnetic field lines in the simulation domain. If both ends of a field line fall within $r < 4\ R_E$, then it is a closed field line; if one end falls within $r < 4\ R_E$ and the other end falls in the solar wind, it is a semi-open field line; otherwise, it is an open field line. The dayside magnetopause, that is, the outer boundary of the magnetosphere, is identified based on the outermost grids with closed field lines (Guo et al., 2023; Yi et al., 2025). For the nightside magnetopause, we identify the magnetopause using the parameter $\beta^* = (P_{\mathrm{th}} + P_{\mathrm{dyn}})/P_{\mathrm{mag}}$, where P_{th}, P_{dyn}, and P_{mag} are the plasma thermal, dynamic, and magnetic pressures, respectively. To define the magnetopause, β^* ranges typically from 0.1 to 1.5 (Guo et al., 2023; Lu et al., 2025; Xu et al., 2016), and here we use $\beta^* = 0.2$. The bow shock is identified by locating the minimum and maximum of the radial (r-direction) gradients of density and velocity in spherical coordinates, respectively.

2.3. Soft X-Ray Intensity

All soft X-ray images shown in this study are derived from the 3-D global hybrid simulation. The soft X-ray intensity I_X is derived by line-of-sight integral of the emissivity PX (Sun et al., 2019, 2020):

$$I_X = \frac{1}{4\pi}\int P_X dr = \frac{1}{4\pi}\int \alpha_X n_H n_{\mathrm{SW}} \sqrt{u_b^2 + u_{\mathrm{th}}^2}\, dr \ \left(\mathrm{keV\ cm^{-2}\ s^{-1}\ sr^{-1}}\right),$$

where α_X denotes the charge-exchange efficiency; $n_H = n_0(10R_E/r)^3$ is the exospheric hydrogen number density; n_{sw} is the solar-wind plasma number density; u_b is the bulk flow speed; and u_{th} is the thermal speed. In accordance with previous studies (Connor & Carter, 2019; Cravens et al., 2001; Fuselier et al., 2020; Sun et al., 2019; Voitcu et al., 2025; Whittaker et al., 2016), the value of α_X and n_0 are set to 1×10^{-15} eV cm^2 and 25 cm^{-3} in this study, respectively.

3. Results

Our simulation demonstrates magnetosheath jets generated by the interaction between an interplanetary discontinuity and Earth's bow shock; this scenario differs from jets formed under steady IMF conditions via the interaction of upstream waves with a quasi-parallel bow shock.

3.1. Overview

Figures 1a–1d show the temporal evolution of the interaction between an interplanetary discontinuity and Earth's magnetosphere. The discontinuity convects southward with the solar wind, and the convective electric field ($-\boldsymbol{V}_{sw} \times \boldsymbol{B}$) on both sides is directed toward the discontinuity (Figure 1a). Upon encountering the bow shock, a hot flow anomaly (HFA) forms in the shock-discontinuity interaction (SDI) region (Figure 1b). HFAs are transient structures that form when an interplanetary discontinuity intersects the bow shock under a focusing motional electric field, producing a hot, tenuous core with reduced magnetic-field magnitude and dynamic pressure (Lin, 2002; Lin et al., 2022; Omidi & Sibeck, 2007; Schwartz et al., 1985). Two magnetosheath high-speed jets with enhanced dynamic pressure flank the HFA core. Within the SDI region, the bow shock exhibits large-scale deformation and bulges sunward. At this time, the magnetopause shows no clear response or distortion because the HFA core and the associated magnetosheath jets remain too small (Figure 1b and Figure S1b in

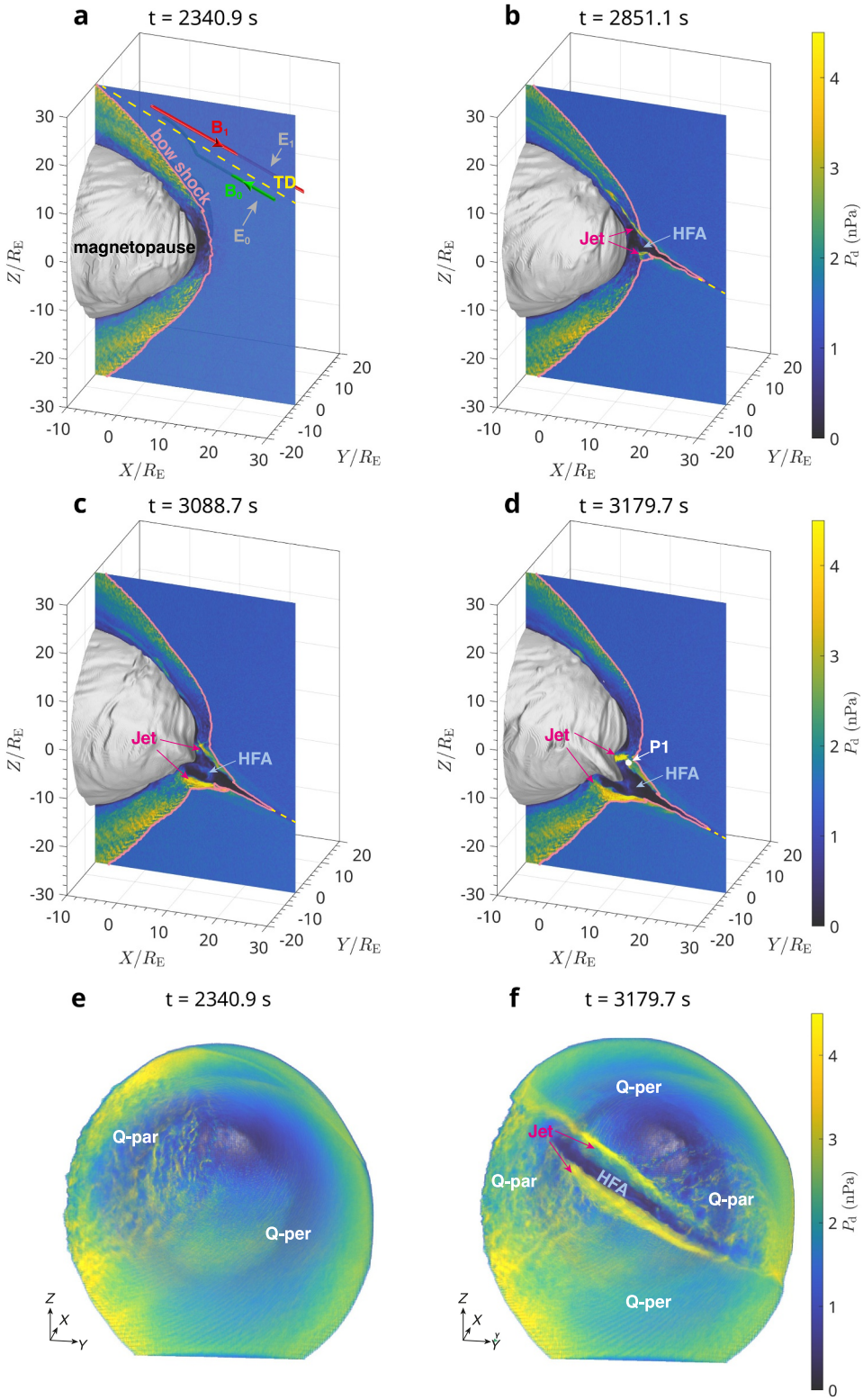

Figure 1. Overview of the magnetosheath jets and HFA formed by SDI. Panels (a–d) show dynamic pressure P_d in $y = -4.4\ R_E$ slice at t = 2,340.9, 2,851.1, 3,088.7, and 3,179.7 s. The 3-D gray surface is the magnetopause, and the pink curve indicate the bow shock. The yellow dashed line highlights the position of TD. Green and red arrowed curves denote magnetic field lines on the pre- and post-TD sides, respectively. Gray arrows indicate the convective electric field directed toward the discontinuity in the solar wind. Panels (e–f) show volume render of dynamic pressure P_d in the magnetosheath at t = 2,340.9 and 3,179.7 s. The red and cyan arrows indicate the magnetosheath jets and HFA, respectively. The white dot in panel (d) indicates the location of the virtual spacecraft.

Supporting Information S1). Some small-scale, periodic undulations of the magnetopause may be signatures of the magnetopause surface eigenmode (Archer et al., 2019). As the discontinuity continues to convect southward, the HFA grows in size (Figures 1c and 1d). At t = 3,179.7 s, the overall HFA's width reaches ∼12 R_E (Figure 1d). By comparison with the pre-SDI magnetopause, magnetosheath jets impinge on and dent the magnetopause, while the low-pressure core draws it sunward, producing large-scale magnetopause distortion (Figures 1d and 2a), consistent with previous observational and simulation studies (Zhang et al., 2022; Zhou et al., 2026). The magnetopause distortion reaches up to 5 R_E in amplitude and extending up to 17 R_E along the discontinuity, and it can propagate across the cusp region to the nightside (see Figure S1 in Supporting Information S1 and Movie S1).

Figures 1e and 1f show the magnetosheath dynamic pressure before and after the SDI. At t = 2,340.9 s (Figure 1e), the dawnside magnetosheath in the Northern Hemisphere is downstream of a quasi-parallel bow shock and exhibits a honeycomb-like structure (Fatemi et al., 2024; Ren, Guo, et al., 2024), whereas elsewhere the magnetosheath is downstream of a quasi-perpendicular bow shock. At t = 3,179.7 s (Figure 1f), the low-latitude magnetosheath is downstream of a quasi-parallel bow shock, whereas the high-latitude magnetosheath is downstream of a quasi-perpendicular bow shock. The HFA develops into a fissure-like structure that spans the entire dayside magnetosheath and extends for approximately 40 R_E along the discontinuity (Figure 1f). The magnetosheath jets are ribbon-like structures that surround the HFA core downstream of both quasi-parallel and quasi-perpendicular portions of the bow shock (Figures 1d and 1f). Because the convective electric field directed toward the discontinuity is stronger at the leading edge (E_0 = 1.45 mV/m) than at the trailing edge (E_1 = 1.18 mV/m), the leading-edge jet is correspondingly larger and stronger, exhibiting higher dynamic pressure than its trailing-edge counterpart.

3.2. Mechanism of Magnetosheath Jet Formation During the SDI

For a high-Mach-number shock, the Rankine–Hugoniot (R-H) jump conditions imply $V_{n,\mathrm{up}} = r_c V_{n,\mathrm{down}}$ and that $V_{t,up}$ is approximately equal to $V_{t,\mathrm{down}}$. Here V_n and V_t are the velocity components normal and tangential to the shock surface, the subscripts "up" and "down" denote upstream and downstream, and r_c is the compression ratio. In our simulation, r_c is about 3.8. Figure 2a shows the velocity magnitude and streamlines in the vicinity of the SDI. As the solar wind crosses the bow shock, its normal velocity component is reduced, whereas the tangential component changes little, deflecting the flow along the shock surface (Figure 2b). Because the upstream flow has a small normal component, the downstream bulk velocity is not appreciably reduced. Additionally, expansion of the low-pressure HFA core compresses the surrounding plasma (Figure 2c), thereby generating magnetosheath jets characterized by enhanced dynamic pressure. Within the magnetosheath jets, strong earthward flows, nearly aligned with the local magnetic field, impinge directly on the magnetopause (Figure 2d). In contrast, the flow in the HFA core is sunward, creating pronounced velocity shear at the core–jet interface (Figure 2d). Two jet-associated vortices form near the magnetopause (Figure 2a), which we attribute to the jets being deflected as they impinge on the magnetopause. However, we do not find clear vortices driven by Kelvin–Helmholtz instability (KHI) along the jet flanks. Its absence may reflect stabilization by a flow-aligned magnetic-field component of magnetic field or the finite resolution of our simulation, which cannot resolve smaller-scale vortices (e.g., electron-scale KHI).

3.3. Virtual Spacecraft Observations

Figure 3 presents observations from a stationary virtual spacecraft fixed at P1 = (10.6, −4.4, −6) R_E (marked by the white dot in Figures 1 and 2). At $t \approx$ 2,980 s, the virtual spacecraft observes the first SDI-generated magnetosheath jet, with dynamic pressure exceeding half the solar-wind dynamic pressure, lasting about 30 s. This is followed by passage of the HFA core for roughly 156 s, and finally by a second SDI-generated magnetosheath jet lasting about 78 s. The normal propagation speed of the discontinuity is $\boldsymbol{V}_{\mathrm{SW}} \cdot \boldsymbol{n}$ = 179 km/s. The three structures (jet-core-jet) encountered sequentially by the virtual spacecraft have extents of 0.8, 4.4, and 2.2 R_E, respectively, along the discontinuity normal (overall 7.4 R_E). Note that, in this case, the leading-edge jet appears smaller than the trailing-edge jet because the virtual spacecraft observes the leading-edge jet at an early stage of its evolution. A direct measurement from the 3-D simulation at t = 3,179.7 s gives an overall HFA extent of 9.8 R_E along the discontinuity normal, exceeding the observation-based estimate of 7.4 R_E. The remaining difference arises from HFA expansion during the observation interval of the virtual spacecraft.

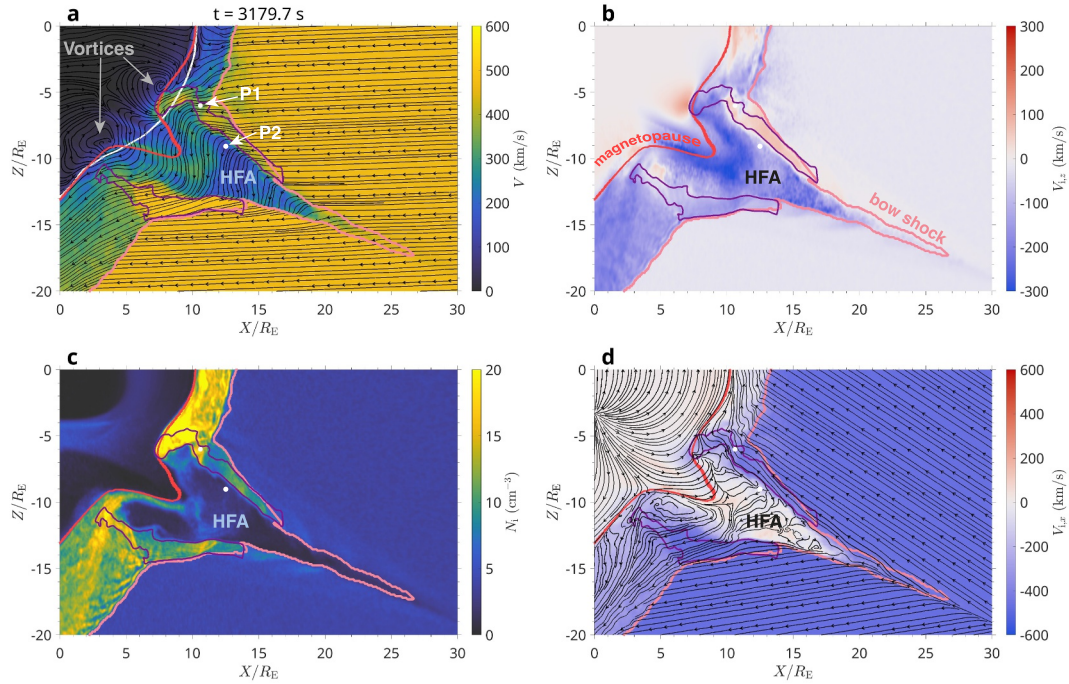

Figure 2. Formation mechanism of magnetosheath jets. Panels (a–d) show ion velocity V, z component of ion velocity $V_{i,z}$, ion density N_i, and x component of ion velocity $V_{i,x}$ in $y = -4.4\ R_E$ slice at $t = 3{,}179.7$ s. The red and pink curves indicate the magnetopause and the bow shock, respectively. The white curves in panel (a) indicate the magnetopause at $t = 2{,}340.9$ s, prior to the SDI. The purple contours mark the jet boundaries, defined as the region where the magnetosheath dynamic pressure exceeds 1.5 times the background value. Black arrowed curves in panel (a) depict velocity streamlines, whereas those in panel (d) depict magnetic field lines. The white dots indicate the location of the virtual spacecraft.

Within magnetosheath jets, the dynamic pressure is enhanced, accompanied by increases in magnetic field strength and bulk velocity (cyan shadings in Figure 3). By contrast, the HFA core exhibits reduced dynamic pressure, plasma density, magnetic field, and bulk velocity (red shading in Figure 3). Because the virtual spacecraft at P1 remains in the magnetosheath before and after the HFA encounter, the density enhancement within the jet (the compressed edge of the HFA) is not obvious. In contrast, the virtual spacecraft at P2 = (12.5, −4.4, −9) R_E (Figure S2 in Supporting Information S1) is in the solar wind before and after the HFA encounter and therefore observes a clear density enhancement in the jet, consistent with previous studies (Kim et al., 2025; Raptis et al., 2025; Sibeck et al., 2021; Suni et al., 2025). In Figure 3c, the jets show a pronounced enhancement of $-V_x$ (earthward flow), whereas the HFA core shows a pronounced enhancement of $+V_x$ (sunward flow). The jet dynamic pressure reaches ∼6.7 nPa, while that in the HFA core drops to ∼0.04 nPa—approximately 5 times and 0.03 times the magnetosheath background (∼1.2 nPa, red solid line in Figure 3d), respectively—thereby driving the large-scale magnetopause distortion.

4. Discussion

Since the discovery of solar wind charge exchange (SWCX) X-ray emission (Cravens, 1997; Lisse et al., 1996), soft X-ray imaging has been proposed as a remote-sensing technique to detect large-scale magnetospheric structures (Branduardi-Raymont et al., 2011; Walsh et al., 2016). SWCX occurs when highly charged solar-wind ions (e.g., O^{7+}) exchange electrons with neutral atoms (e.g., H), placing the ions in excited states that emit soft X-ray photons upon de-excitation. Emissivity is strongest where both ions and neutrals are abundant, notably in the magnetosheath and the cusps. The HFA core and its flanking jets drive a large-scale reconfiguration of the magnetosheath and may be detectable by soft X-ray imagers via SWCX emission. Figure 4 presents synthetic X-ray images for a lunar-based soft X-ray imager (LSXI, Guo et al., 2021), derived from the simulation data. The soft X-ray emissivity peaks in the magnetosheath and the cusps (Figure 4a). During the SDI, it is depressed in the HFA core but enhanced in the flanking magnetosheath jets (Figure 4b). Real-time soft X-ray images indicate that, prior to the SDI, the magnetosheath X-ray intensity is relatively uniform (Figure 4c). After SDI onset, a

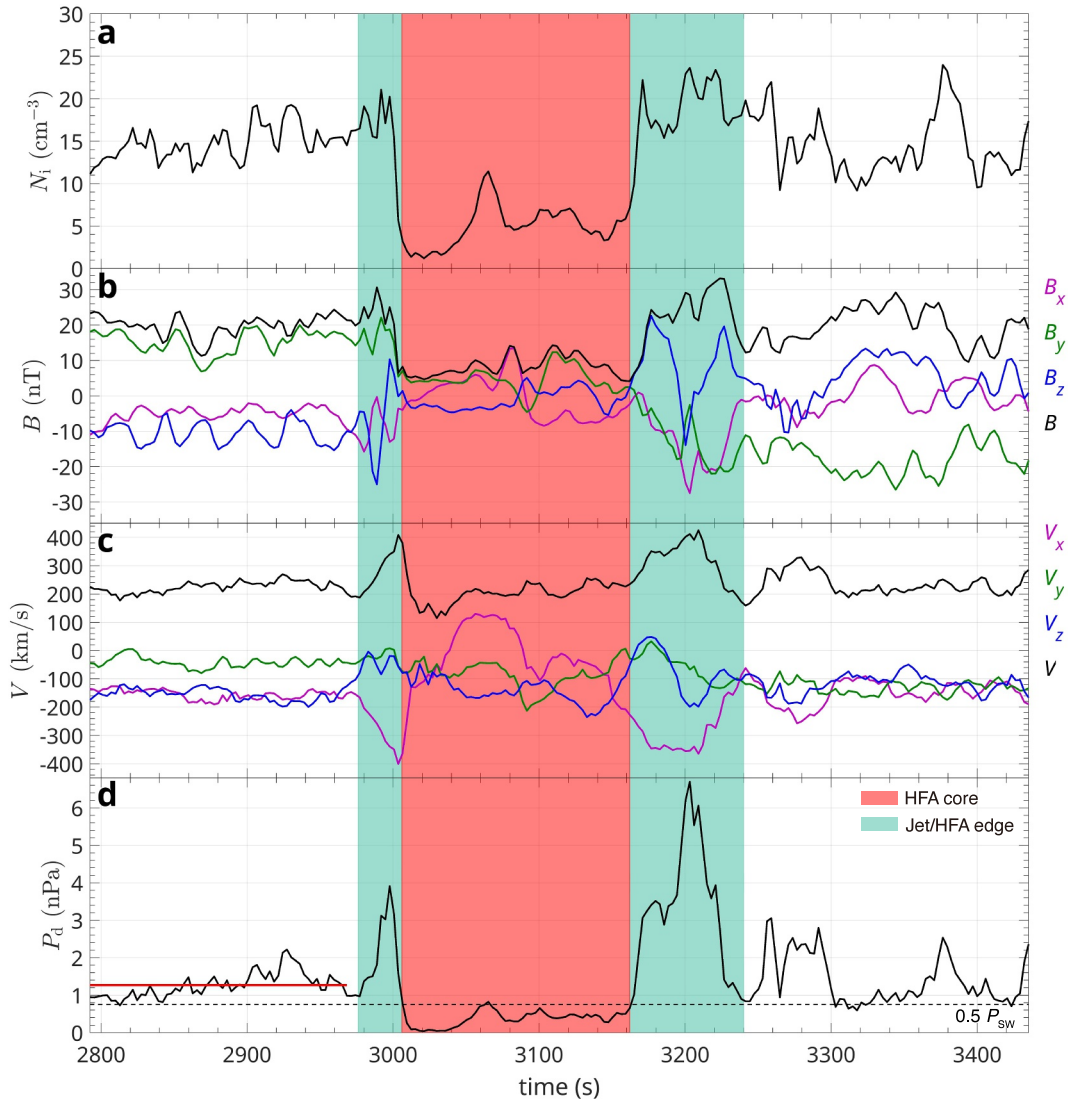

Figure 3. Virtual spacecraft observations of magnetosheath jets and HFA. Panels (a–d) show ion density, magnetic fields, ion velocity, and dynamic pressure measured by a stationary virtual spacecraft (indicated in Figure 1d) at P1 = (10.6, −4.4, −6) R_E. The red and cyan shadings mark the HFA core and magnetosheath jets, respectively. The red solid and black dotted lines in panel (d) denote half the dynamic pressure in the solar wind and the mean background magnetosheath dynamic pressure, respectively.

pronounced intensity cavity appears at the HFA core, flanked by regions of enhanced X-ray intensity that correspond to the jets (Figure 4d). Ten-minute averages of the soft X-ray intensity clearly resolve the SDI-driven structures (Figures 4e and 4h). Although realistic SXI noise degrades the image quality (Figures 4f and 4i), median filtering recovers these structures (Figures 4g and 4j). We suggest that SDI-driven structures should be detectable by future soft X-ray imagers.

Under steady solar wind conditions, Hietala et al. (2009) proposed that local curvature variations of the quasi-parallel bow shock create regions where the upstream flow is nearly perpendicular to the local shock normal, so the shock primarily deflects the flow along its surface with little deceleration, producing jets. However, Ren et al. (2023) suggest that rapid, transient bow-shock undulations cannot maintain continuous jet production. Our results indicate that SDIs produce persistent bow-shock deformations, with the ensuing jets consistent with Hietala et al. (2009) and corroborating the scenario of Zhou et al. (2023, 2026), which is based on an observation-derived 3-D reconstruction of the bow shock. In some cases, a rotational discontinuity can also generate an HFA under the same focusing geometry (Turc et al., 2025). The interactions between rotational discontinuity and the

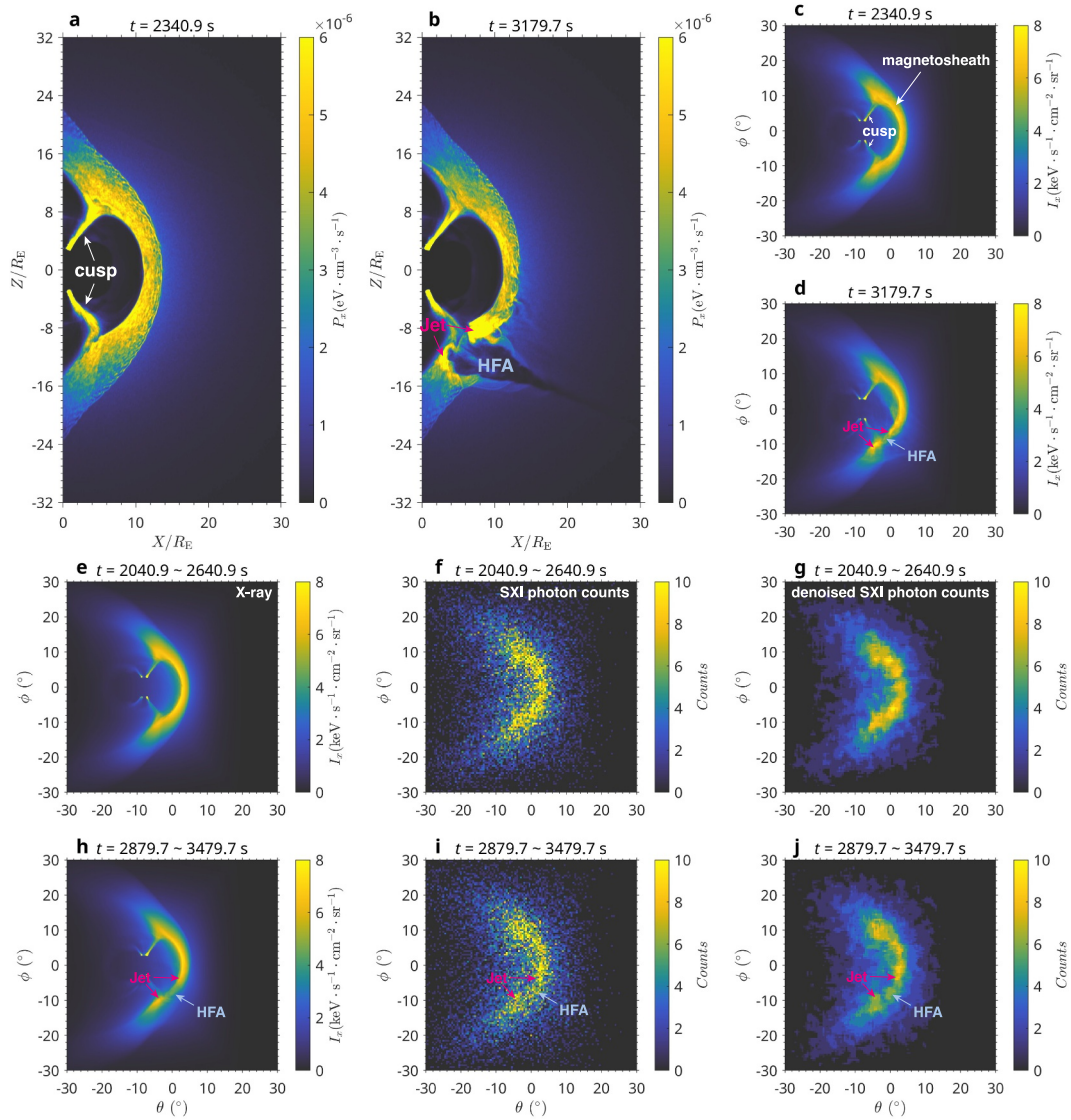

Figure 4. X-ray image from a lunar-based soft X-ray imager located at $(0, -60, 0)$ R_E. Panels (a, b) show X-ray emissivity P_X in the meridian plane at $t = 2{,}340.9$ and 3,179.7 s. Panels (c, d) show X-ray intensity I_X at $t = 2{,}340.9$ and 3,179.7 s. The white arrows indicate the north and south cusps. Panels (e, h) show the average X-ray intensity over 10 min before and after the formation of HFA. Panels (f, i) show SXI instrument-simulated images with realistic noise added (Guo, Sun, et al., 2022), corresponding to panel e and h, respectively. Panels (g, j) perform median filtering of the images (f, i) in two dimensions. The cyan arrows indicate the HFA.

bow shock can also generate magnetosheath jets (Suni et al., 2025), some of which may represent reconnection outflows (Lu et al., 2020). Previous observations have reported the occurrence of jets downstream of quasi-perpendicular shock (Blanco-Cano et al., 2023; Goncharov et al., 2020; Kajdič et al., 2021; Raptis et al., 2020). Our results indicate that SDI-driven jets can extend across both the quasi-perpendicular and quasi-parallel magnetosheath, consistent with previously proposed jet-formation mechanisms in the quasi-perpendicular magnetosheath associated with solar-wind discontinuities (Archer et al., 2012; Zhou et al., 2026).

Previous studies showed that the low-pressure HFA core draws the magnetopause outward (Archer et al., 2014; Sibeck et al., 1999). Recently, Sibeck et al. (2025) performed a global MHD simulation in which a solar-wind slab with reduced density and magnetic field strengths, but enhanced temperatures interacts with Earth's bow shock and magnetosphere, producing a growing transient at the bow shock with HFA-like properties and an outward magnetopause bulges. We perform a 3-D global hybrid simulation with kinetic ions that self-consistently

reproduces the SDI, the HFA with flanking jets, and their impacts on the magnetopause. The simulation provides a more realistic 3-D physical picture of SDI-driven jet formation and the resulting magnetopause distortion.

5. Conclusions

We used a 3-D global hybrid simulation to study magnetosheath jets formed by SDIs and their impact on the magnetopause. SDI-driven deformation of the bow shock redirects the solar wind according to the R-H relations, deflecting the flow along the shock with little deceleration, while expansion of the low-pressure HFA core compresses the flanks. Together, these processes produce ribbon-like jets extending along the discontinuity downstream of both quasi-parallel and quasi-perpendicular portions of the bow shock. The HFA grows into a fissure-like structure spanning the dayside magnetosheath, reaching ∼40 R_E along the discontinuity and ∼10 R_E along the discontinuity normal. Dynamic pressure in jets reaches ∼7 nPa, whereas it drops to ∼0.1 nPa in the HFA core. These pressure contrasts drive large-scale magnetopause responses: outward protrusion over the HFA core and indentation at the jets, with distortion amplitudes up to ∼5 R_E and along-discontinuity extents of ∼17 R_E. The distortion convects with the discontinuity. Synthetic soft X-ray images derived from the simulation indicate that the SDI-drive structures should be detectable by future soft X-ray imagers, such as the lunar-based soft X-ray imager (Guo et al., 2021).

Conflict of Interest

The authors declare no conflicts of interest relevant to this study.

Availability Statement

The simulation data (J. Guo, 2025) used to plot the figures in this study can be download from "National Space Science Data Center, National Science and Technology Infrastructure of China".

Acknowledgments
This research was funded by the National Natural Science Foundation of China (42508011, 42274196, 42174181, 424B2031, and 42404163), the Strategic Priority Research Program of Chinese Academy of Sciences (XDB0560000), the National Key Research and Development Program of China (2022YFA1604600), the Fundamental Research Funds for the Central Universities (WK2080250226), the China Postdoctoral Science Foundation (GZB20250097 and 2025M770380), and the Xiaomi Young Talents Program. Computer resources were provided by the Hefei Advanced Computing Center of China.

References

Archer, M. O., Hietala, H., Hartinger, M. D., Plaschke, F., & Angelopoulos, V. (2019). Direct observations of a surface Eigenmode of the dayside magnetopause. *Nature Communications*, *10*(1), 615. https://doi.org/10.1038/s41467-018-08134-5

Archer, M. O., & Horbury, T. S. (2013). Magnetosheath dynamic pressure enhancements: Occurrence and typical properties. *Annales Geophysicae*, *31*(2), 319–331. https://doi.org/10.5194/angeo-31-319-2013

Archer, M. O., Horbury, T. S., & Eastwood, J. P. (2012). Magnetosheath pressure pulses: Generation downstream of the bow shock from solar wind discontinuities. *Journal of Geophysical Research*, *117*(A5). https://doi.org/10.1029/2011ja017468

Archer, M. O., Turner, D. L., Eastwood, J. P., Horbury, T. S., & Schwartz, S. J. (2014). The role of pressure gradients in driving sunward magnetosheath flows and magnetopause motion. *Journal of Geophysical Research: Space Physics*, *119*(10), 8117–8125. https://doi.org/10.1002/2014ja020342

Bale, S., Balikhin, M., Horbury, T., Krasnoselskikh, V., Kucharek, H., Möbius, E., et al. (2005). Quasi-perpendicular shock structure and processes. *Space Science Reviews*, *118*(1), 161–203. https://doi.org/10.1007/s11214-005-3827-0

Balogh, A., & Treumann, R. A. (2013). *Physics of collisionless shocks: Space plasma shock waves*. Springer Science & Business Media. Retrieved from https://books.google.com/books?id=mR4_AAAAQBAJ

Blanco-Cano, X., Rojas-Castillo, D., Kajdic, P., & Preisser, L. (2023). Jets and mirror mode waves in Earth's magnetosheath. *Journal of Geophysical Research: Space Physics*, *128*(7), e2022JA031221. https://doi.org/10.1029/2022JA031221

Branduardi-Raymont, G., Sembay, S. F., Eastwood, J. P., Sibeck, D. G., Abbey, T. A., Brown, P., et al. (2011). AXIOM: Advanced X-ray imaging of the magnetosphere. *Experimental Astronomy*, *33*(2–3), 403–443. https://doi.org/10.1007/s10686-011-9239-0

Burgess, D., Möbius, E., & Scholer, M. (2012). Ion acceleration at the Earth's bow shock. *Space Science Reviews*, *173*(1), 5–47. https://doi.org/10.1007/s11214-012-9901-5

Cao, J., Fu, H., Zhang, T., Reme, H., Dandouras, I., & Lucek, E. (2009). Direct evidence of solar wind deceleration in the foreshock of the Earth. *Journal of Geophysical Research*, *114*(A2). https://doi.org/10.1029/2008ja013524

Connor, H. K., & Carter, J. A. (2019). Exospheric neutral hydrogen density at the nominal 10 RE subsolar point deduced from XMM-Newton X-ray observations. *Journal of Geophysical Research: Space Physics*, *124*(3), 1612–1624. https://doi.org/10.1029/2018ja026187

Cravens, T. E. (1997). Comet Hyakutake X-ray source: Charge transfer of solar wind heavy ions. *Geophysical Research Letters*, *24*(1), 105–108. https://doi.org/10.1029/96gl03780

Cravens, T. E., Robertson, I. P., & Snowden, S. L. (2001). Temporal variations of geocoronal and heliospheric X-ray emission associated with the solar wind interaction with neutrals. *Journal of Geophysical Research*, *106*(A11), 24883–24892. https://doi.org/10.1029/2000ja000461

Dmitriev, A. V., & Suvorova, A. V. (2015). Large-scale jets in the magnetosheath and plasma penetration across the magnetopause: THEMIS observations. *Journal of Geophysical Research: Space Physics*, *120*(6), 4423–4437. https://doi.org/10.1002/2014ja020953

Escoubet, C. P., Hwang, K. J., Toledo-Redondo, S., Turc, L., Haaland, S. E., Aunai, N., et al. (2020). Cluster and MMS simultaneous observations of magnetosheath high speed jets and their impact on the magnetopause. *Frontiers in Astronomy and Space Sciences*, *6*, 78. https://doi.org/10.3389/fspas.2019.00078

Fatemi, S., Hamrin, M., Krämer, E., Gunell, H., Nordin, G., Karlsson, T., & Goncharov, O. (2024). Unveiling the 3D structure of magnetosheath jets. *Monthly Notices of the Royal Astronomical Society*, *531*(4), 4692–4713. https://doi.org/10.1093/mnras/stae1456

Fu, H.-S., Cao, J.-B., Yang, B., Lucek, E., Rème, H., & Dandouras, I. (2009). ULF waves associated with solar wind deceleration in the Earth's foreshock. *Chinese Physics Letters*, *26*(11), 119402. https://doi.org/10.1088/0256-307X/26/11/119402

Fuselier, S. A., Dayeh, M. A., Galli, A., Funsten, H. O., Schwadron, N. A., Petrinec, S. M., et al. (2020). Neutral atom imaging of the solar wind-magnetosphere-exosphere interaction near the subsolar magnetopause. *Geophysical Research Letters*, *47*(19), e2020GL089362. https://doi.org/10.1029/2020GL089362

Goncharov, O., Gunell, H., Hamrin, M., & Chong, S. (2020). Evolution of high-speed jets and plasmoids downstream of the quasi-perpendicular bow shock. *Journal of Geophysical Research: Space Physics*, *125*(6), e2019JA027667. https://doi.org/10.1029/2019ja027667

Gunell, H., Hamrin, M., Nesbit-Östman, S., Krämer, E., & Nilsson, H. (2023). Magnetosheath jets at Mars. *Science Advances*, *9*(22), eadg5703. https://doi.org/10.1126/sciadv.adg5703

Guo, A., Lu, Q., Lu, S., Yang, Z., & Gao, X. (2024a). Electron shock drift acceleration at a low-Mach-number, low-plasma-beta quasi-perpendicular shock. *The Astrophysical Journal*, *974*(1), 57. https://doi.org/10.3847/1538-4357/ad6c46

Guo, J. (2025). Data for SDI-driven magnetosheath jets (Version V1) [Dataset]. https://doi.org/10.57760/sciencedb.33635

Guo, J., Lu, S., Lu, Q., Lin, Y., Wang, X., Ren, J., et al. (2022). Large-scale high-speed jets in Earth's magnetosheath: Global hybrid simulations. *Journal of Geophysical Research: Space Physics*, *127*(6), e2022JA030477. https://doi.org/10.1029/2022ja030477

Guo, J., Lu, S., Lu, Q., Ren, J., Ma, J., Slavin, J. A., et al. (2024). Three-dimensional global hybrid simulation of magnetosheath jets at mercury. *The Astrophysical Journal Letters*, *978*(1), L9. https://doi.org/10.3847/2041-8213/ad9dd7

Guo, J., Lu, S., Lu, Q., Slavin, J. A., Sun, W., Ren, J., et al. (2023). Three-dimensional global hybrid simulations of mercury's disappearing dayside magnetosphere. *Journal of Geophysical Research: Planets*, *128*(12), e2023JE008032. https://doi.org/10.1029/2023je008032

Guo, J., Lu, S., Lu, Q., Wang, B., Wang, S., Ren, J., et al. (2026). Large-scale distortion of the dayside magnetopause under radial interplanetary magnetic field. *Science Bulletin*. https://doi.org/10.1016/j.scib.2026.01.032

Guo, Y., Sun, T., Wang, C., & Sembay, S. (2022). Deriving the magnetopause position from wide field-of-view soft X-ray imager simulation. *Science China Earth Sciences*, *65*(8), 1601–1611. https://doi.org/10.1007/s11430-021-9937-y

Guo, Y., Wang, C., Wei, F., Sun, T., Yu, X., Peng, S., et al. (2021). A Lunar-based soft X-ray imager (LSXI) for the Earth's magnetosphere. *Science China Earth Sciences*, *64*(7), 1026–1035. https://doi.org/10.1007/s11430-020-9792-5

Han, D. S., Hietala, H., Chen, X. C., Nishimura, Y., Lyons, L. R., Liu, J. J., et al. (2017). Observational properties of dayside throat aurora and implications on the possible generation mechanisms. *Journal of Geophysical Research: Space Physics*, *122*(2), 1853–1870. https://doi.org/10.1002/2016ja023394

Hao, Y., Lu, Q., Wu, D., Lu, S., Xiang, L., & Ke, Y. (2021). Low-frequency waves upstream of quasi-parallel shocks: Two-dimensional hybrid simulations. *The Astrophysical Journal*, *915*(1), 64. https://doi.org/10.3847/1538-4357/ac02ce

Hietala, H., Laitinen, T. V., Andreeova, K., Vainio, R., Vaivads, A., Palmroth, M., et al. (2009). Supermagnetosonic jets behind a collisionless quasiparallel shock. *Physical Review Letters*, *103*(24), 245001. https://doi.org/10.1103/PhysRevLett.103.245001

Hietala, H., Partamies, N., Laitinen, T. V., Clausen, L. B. N., Facskó, G., Vaivads, A., et al. (2012). Supermagnetosonic subsolar magnetosheath jets and their effects: From the solar wind to the ionospheric convection. *Annales Geophysicae*, *30*(1), 33–48. https://doi.org/10.5194/angeo-30-33-2012

Hietala, H., Phan, T. D., Angelopoulos, V., Oieroset, M., Archer, M. O., Karlsson, T., & Plaschke, F. (2018). In situ observations of a magnetosheath high-speed jet triggering magnetopause reconnection. *Geophysical Research Letters*, *45*(4), 1732–1740. https://doi.org/10.1002/2017gl076525

Hietala, H., Trotta, D., Fedeli, A., Wilson, L. B., Vuorinen, L., & Coburn, J. T. (2024). Candidates for downstream jets at interplanetary shocks. *Monthly Notices of the Royal Astronomical Society*, *531*(2), 2415–2421. https://doi.org/10.1093/mnras/stae1294

Kajdič, P., Raptis, S., Blanco-Cano, X., & Karlsson, T. (2021). Causes of jets in the quasi-perpendicular magnetosheath. *Geophysical Research Letters*, *48*(13), e2021GL093173. https://doi.org/10.1029/2021gl093173

Karlsson, T., Brenning, N., Nilsson, H., Trotignon, J. G., Vallières, X., & Facsko, G. (2012). Localized density enhancements in the magnetosheath: Three-dimensional morphology and possible importance for impulsive penetration. *Journal of Geophysical Research*, *117*(A3). https://doi.org/10.1029/2011ja017059

Karlsson, T., Kullen, A., Liljeblad, E., Brenning, N., Nilsson, H., Gunell, H., & Hamrin, M. (2015). On the origin of magnetosheath plasmoids and their relation to magnetosheath jets. *Journal of Geophysical Research: Space Physics*, *120*(9), 7390–7403. https://doi.org/10.1002/2015ja021487

Karlsson, T., Liljeblad, E., Kullen, A., Raines, J. M., Slavin, J. A., & Sundberg, T. (2016). Isolated magnetic field structures in mercury's magnetosheath as possible analogues for terrestrial magnetosheath plasmoids and jets. *Planetary and Space Science*, *129*, 61–73. https://doi.org/10.1016/j.pss.2016.06.002

Kim, H., Nakamura, R., Grimmich, N., Settino, A., Hwang, K. J., Park, J., et al. (2025). Extreme magnetopause deformation induced by high-speed jet from foreshock transient. *Geophysical Research Letters*, *52*(20), e2025GL117683. https://doi.org/10.1029/2025gl117683

Kramer, E., Koller, F., Suni, J., LaMoury, A. T., Poppelwerth, A., Glebe, G., et al. (2025). Jets downstream of collisionless shocks: Recent discoveries and challenges. *Space Science Reviews*, *221*(1), 4. https://doi.org/10.1007/s11214-024-01129-3

Krasnoselskikh, V., Balikhin, M., Walker, S., Schwartz, S., Sundkvist, D., Lobzin, V., et al. (2013). The dynamic quasiperpendicular shock: Cluster discoveries. *Space Science Reviews*, *178*(2), 535–598. https://doi.org/10.1007/s11214-013-9972-y

LaMoury, A. T., Hietala, H., Plaschke, F., Vuorinen, L., & Eastwood, J. P. (2021). Solar wind control of magnetosheath jet formation and propagation to the magnetopause. *Journal of Geophysical Research: Space Physics*, *126*(9), e2021JA029592. https://doi.org/10.1029/2021ja029592

Lembege, B., & Savoini, P. (1992). Nonstationarity of a two-dimensional quasiperpendicular supercritical collisionless shock by self-reformation. *Physics of Fluids B: Plasma Physics*, *4*(11), 3533–3548. https://doi.org/10.1063/1.860361

Lin, Y. (2002). Global hybrid simulation of hot flow anomalies near the bow shock and in the magnetosheath. *Planetary and Space Science*, *50*(5–6), 577–591. https://doi.org/10.1016/s0032-0633(02)00037-5

Lin, Y., Wang, X., Sibeck, D. G., Wang, C. P., & Lee, S. H. (2022). Global asymmetries of hot flow anomalies. *Geophysical Research Letters*, *49*(4), e2021GL096970. https://doi.org/10.1029/2021gl096970

Lisse, C. M., Dennerl, K., Englhauser, J., Harden, M., Marshall, F. E., Mumma, M. J., et al. (1996). Discovery of X-ray and extreme ultraviolet emission from comet C/Hyakutake 1996 B2. *Science*, *274*(5285), 205–209. https://doi.org/10.1126/science.274.5285.205

Liu, T. Z., Hietala, H., Angelopoulos, V., Omelchenko, Y., Roytershteyn, V., & Vainio, R. (2019). THEMIS observations of particle acceleration by a magnetosheath jet-driven bow wave. *Geophysical Research Letters*, *46*(14), 7929–7936. https://doi.org/10.1029/2019gl082614

Lu, Q., Guo, J., Lu, S., Wang, X., Slavin, J. A., Sun, W., et al. (2022). Three-dimensional global hybrid simulations of flux transfer event showers at mercury. *The Astrophysical Journal*, *937*(1), 1. https://doi.org/10.3847/1538-4357/ac8bcf

Lu, Q., Ke, Y., Wang, X., Liu, K., Gao, X., Chen, L., & Wang, S. (2019). Two-dimensional gcPIC simulation of rising-tone chorus waves in a dipole magnetic field. *Journal of Geophysical Research: Space Physics*, *124*(6), 4157–4167. https://doi.org/10.1029/2019ja026586

Lu, Q., Wang, H., Wang, X., Lu, S., Wang, R., Gao, X., & Wang, S. (2020). Turbulence-driven magnetic reconnection in the magnetosheath downstream of a quasi-parallel shock: A three-dimensional global hybrid simulation. *Geophysical Research Letters*, *47*(1), e2019GL085661. https://doi.org/10.1029/2019gl085661

Lu, S., Guo, J., Lu, Q., Shu, Y., Ren, J., Wang, R., & Hajra, R. (2025). Three-dimensional global hybrid simulations of plasma transport and energy conversion during solar wind-magnetosphere interactions. *Geophysical Research Letters*, *52*(17), e2025GL117084. https://doi.org/10.1029/2025gl117084

Ma, J., Tang, B., Gao, X., Li, W., Lu, Q., Guo, W., et al. (2024). The comprehensive response of the magnetopause to the impact of an isolated magnetosheath high-speed jet. *Geophysical Research Letters*, *51*(21), e2024GL111132. https://doi.org/10.1029/2024gl111132

Němeček, Z., Šafránková, J., Grygorov, K., Mokrý, A., Pi, G., Aghabozorgi Nafchi, M., et al. (2023). Extremely distant magnetopause locations caused by magnetosheath jets. *Geophysical Research Letters*, *50*(24), e2023GL106131. https://doi.org/10.1029/2023gl106131

Němeček, Z., Šafránková, J., Přech, L., Sibeck, D., Kokubun, S., & Mukai, T. (1998). Transient flux enhancements in the magnetosheath. *Geophysical Research Letters*, *25*(8), 1273–1276. https://doi.org/10.1029/98gl50873

Nykyri, K., Bengtson, M., Angelopoulos, V., Nishimura, Y., & Wing, S. (2019). Can enhanced flux loading by high-speed jets lead to a substorm? Multipoint detection of the Christmas day substorm onset at 08:17 UT, 2015. *Journal of Geophysical Research: Space Physics*, *124*(6), 4314–4340. https://doi.org/10.1029/2018ja026357

Omidi, N., & Sibeck, D. G. (2007). Formation of hot flow anomalies and solitary shocks. *Journal of Geophysical Research*, *112*(A1). https://doi.org/10.1029/2006ja011663

Palmroth, M., Hietala, H., Plaschke, F., Archer, M., Karlsson, T., Blanco-Cano, X., et al. (2018). Magnetosheath jet properties and evolution as determined by a global hybrid-Vlasov simulation. *Annales Geophysicae*, *36*(5), 1171–1182. https://doi.org/10.5194/angeo-36-1171-2018

Plaschke, F., Hietala, H., & Angelopoulos, V. (2013). Anti-sunward high-speed jets in the subsolar magnetosheath. *Annales Geophysicae*, *31*(10), 1877–1889. https://doi.org/10.5194/angeo-31-1877-2013

Plaschke, F., Hietala, H., Angelopoulos, V., & Nakamura, R. (2016). Geoeffective jets impacting the magnetopause are very common. *Journal of Geophysical Research: Space Physics*, *121*(4), 3240–3253. https://doi.org/10.1002/2016JA022534

Plaschke, F., Hietala, H., Archer, M., Blanco-Cano, X., Kajdic, P., Karlsson, T., et al. (2018). Jets downstream of collisionless shocks. *Space Science Reviews*, *214*(5), 81. https://doi.org/10.1007/s11214-018-0516-3

Pöppelwerth, A., Glebe, G., Mieth, J. Z. D., Koller, F., Karlsson, T., Vörös, Z., & Plaschke, F. (2024). Scale size estimation and flow pattern recognition around a magnetosheath jet. *Annales Geophysicae*, *42*(1), 271–284. https://doi.org/10.5194/angeo-42-271-2024

Qiu, H. X., Han, D. S., Shi, R., & Liu, J. (2024). Magnetosheath high-speed jet drives multiple auroral arcs near local noon. *AGU Advances*, *5*(5), e2024AV001197. https://doi.org/10.1029/2024av001197

Raptis, S., Karlsson, T., Plaschke, F., Kullen, A., & Lindqvist, P. A. (2020). Classifying magnetosheath jets using MMS: Statistical properties. *Journal of Geophysical Research: Space Physics*, *125*(11), e2019JA027754. https://doi.org/10.1029/2019ja027754

Raptis, S., Karlsson, T., Vaivads, A., Pollock, C., Plaschke, F., Johlander, A., et al. (2022). Downstream high-speed plasma jet generation as a direct consequence of shock reformation. *Nature Communications*, *13*(1), 598. https://doi.org/10.1038/s41467-022-28110-4

Raptis, S., Lindberg, M., Liu, T. Z., Turner, D. L., Lalti, A., Zhou, Y., et al. (2025). Multimission observations of relativistic electrons and high-speed jets linked to shock-generated transients. *The Astrophysical Journal Letters*, *981*(1), L10. https://doi.org/10.3847/2041-8213/adb154

Ren, J., Guo, J., Lu, Q., Lu, S., Gao, X., Ma, J., & Wang, R. (2024). Honeycomb-like magnetosheath structure formed by jets: Three-dimensional global hybrid simulations. *Geophysical Research Letters*, *51*(12), e2024GL109925. https://doi.org/10.1029/2024gl109925

Ren, J., Lu, Q., Gao, X., Gedalin, M., Qiu, H., Han, D., & Wang, R. (2024). Hybrid simulation of magnetosheath jet-driven bow waves. *Geophysical Research Letters*, *51*(5), e2023GL106606. https://doi.org/10.1029/2023gl106606

Ren, J., Lu, Q., Guo, J., Gao, X., Lu, S., Wang, S., & Wang, R. (2023). Two-dimensional hybrid simulations of high-speed jets downstream of quasi-parallel shocks. *Journal of Geophysical Research: Space Physics*, *128*(8), e2023JA031699. https://doi.org/10.1029/2023ja031699

Schwartz, S. J., Chaloner, C. P., Christiansen, P. J., Coates, A. J., Hall, D. S., Johnstone, A. D., et al. (1985). An active current sheet in the solar wind. *Nature*, *318*(6043), 269–271. https://doi.org/10.1038/318269a0

Shan, L., Du, A., Tsurutani, B. T., Ge, Y. S., Lu, Q., Mazelle, C., et al. (2020). In situ observations of the formation of periodic collisionless plasma shocks from fast mode waves. *The Astrophysical Journal Letters*, *888*(2), L17. https://doi.org/10.3847/2041-8213/ab5db3

Sibeck, D., Borodkova, N., Schwartz, S., Owen, C., Kessel, R., Kokubun, S., et al. (1999). Comprehensive study of the magnetospheric response to a hot flow anomaly. *Journal of Geophysical Research*, *104*(A3), 4577–4593. https://doi.org/10.1029/1998JA900021

Sibeck, D. G., Lee, S. H., Omidi, N., & Angelopoulos, V. (2021). Foreshock cavities: Direct transmission through the bow shock. *Journal of Geophysical Research: Space Physics*, *126*(5), e2021JA029201. https://doi.org/10.1029/2021ja029201

Sibeck, D. G., Rastätter, L., & El Alaoui, M. (2025). Using a magnetohydrodynamic (MHD) model to simulate the magnetospheric response to a kinetic foreshock transient. *Geophysical Research Letters*, *52*(5), e2024GL113463. https://doi.org/10.1029/2024gl113463

Su, Y., Lu, Q., Huang, C., Wu, M., Gao, X., & Wang, S. (2012). Particle acceleration and generation of diffuse superthermal ions at a quasi-parallel collisionless shock: Hybrid simulations. *Journal of Geophysical Research*, *117*(A8). https://doi.org/10.1029/2012ja017736

Sun, J., Ren, J., Lu, Q., Zhang, B., & Yang, H. (2024). The transmission of Pc 3 waves from the foreshock into the Earth's magnetosphere: 3D global hybrid simulation. *Journal of Geophysical Research: Space Physics*, *129*(10), e2024JA033007. https://doi.org/10.1029/2024ja033007

Sun, T., Wang, C., Connor, H. K., Jorgensen, A. M., & Sembay, S. (2020). Deriving the magnetopause position from the soft X-ray image by using the tangent fitting approach. *Journal of Geophysical Research: Space Physics*, *125*(9), e2020JA028169. https://doi.org/10.1029/2020ja028169

Sun, T. R., Wang, C., Sembay, S. F., Lopez, R. E., Escoubet, C. P., Branduardi-Raymont, G., et al. (2019). Soft X-ray imaging of the magnetosheath and cusps under different solar wind conditions: MHD simulations. *Journal of Geophysical Research: Space Physics*, *124*(4), 2435–2450. https://doi.org/10.1029/2018ja026093

Suni, J., Palmroth, M., Turc, L., Battarbee, M., Johlander, A., Tarvus, V., et al. (2021). Connection between foreshock structures and the generation of magnetosheath jets: Vlasiator results. *Geophysical Research Letters*, *48*(20), e2021GL095655. https://doi.org/10.1029/2021gl095655

Suni, J., Palmroth, M., Turc, L., Battarbee, M., Pfau-Kempf, Y., & Ganse, U. (2025). Magnetosheath jets associated with a solar wind rotational discontinuity in a hybrid-Vlasov simulation. *Journal of Geophysical Research: Space Physics*, *130*(6), e2025JA033995. https://doi.org/10.1029/2025ja033995

Tang, H.-B., Hao, Y.-F., Hu, G.-Y., Lu, Q.-M., Ren, C., Zhang, Y., et al. (2025). Laboratory observation of ion drift acceleration via reflection off laser-produced magnetized collisionless shocks. *Science Advances*, *11*(7), eadn3320. https://doi.org/10.1126/sciadv.adn3320

Turc, L., Archer, M. O., Zhou, H., Pfau-Kempf, Y., Suni, J., Kajdič, P., et al. (2025). Interplay between a foreshock bubble and a hot flow anomaly forming along the same rotational discontinuity. *Geophysical Research Letters*, *52*(12), e2025GL116473. https://doi.org/10.1029/2025gl116473

Turc, L., Tarvus, V., Dimmock, A. P., Battarbee, M., Ganse, U., Johlander, A., et al. (2020). Asymmetries in the Earth's dayside magnetosheath: Results from global hybrid-Vlasov simulations. In *Paper presented at annales geophysicae, copernicus publications Göttingen, Germany*. https://doi.org/10.5194/angeo-38-1045-2020

Voitcu, G., Echim, M., Teodorescu, M., & Munteanu, C. (2025). Soft X-ray imaging of dense and fast magnetosheath jets: Numerical simulations. *Earth and Space Science*, *12*(11), e2025EA004798. https://doi.org/10.1029/2025ea004798

Vuorinen, L., Vainio, R., Hietala, H., & Liu, T. Z. (2022). Monte Carlo simulations of electron acceleration at bow waves driven by fast jets in the Earth's Magnetosheath. *The Astrophysical Journal*, *934*(2), 165. https://doi.org/10.3847/1538-4357/ac7f42

Walsh, B. M., Collier, M. R., Kuntz, K. D., Porter, F. S., Sibeck, D. G., Snowden, S. L., et al. (2016). Wide field-of-view soft X-ray imaging for solar wind-magnetosphere interactions. *Journal of Geophysical Research: Space Physics*, *121*(4), 3353–3361. https://doi.org/10.1002/2016ja022348

Wang, B., Nishimura, Y., Hietala, H., Lyons, L., Angelopoulos, V., Plaschke, F., et al. (2018). Impacts of magnetosheath high-speed jets on the magnetosphere and ionosphere measured by optical imaging and satellite observations. *Journal of Geophysical Research: Space Physics*, *123*(6), 4879–4894. https://doi.org/10.1029/2017ja024954

Wang, X., Lu, J., Wang, M., Zhou, Y., & Hao, Y. (2023). Simultaneous observation of magnetopause expansion under radial IMF and indention by HSJ. *Geophysical Research Letters*, *50*(20), e2023GL105270. https://doi.org/10.1029/2023gl105270

Wang, Z., Han, D., Chen, X., Shi, R., Teng, S., Zhang, J., et al. (2024). Observations of a throat aurora directly driven by magnetosheath high-speed jet. *Journal of Geophysical Research: Space Physics*, *130*(1), e2024JA033276. https://doi.org/10.1029/2024ja033276

Whittaker, I. C., Sembay, S., Carter, J. A., Read, A. M., Milan, S. E., & Palmroth, M. (2016). Modeling the magnetospheric X-ray emission from solar wind charge exchange with verification from XMM-Newton observations. *Journal of Geophysical Research: Space Physics*, *121*(5), 4158–4179. https://doi.org/10.1002/2015ja022292

Wu, M., Hao, Y., Lu, Q., Huang, C., Guo, F., & Wang, S. (2015). The role of large amplitude upstream low-frequency waves in the generation of superthermal ions at a quasi-parallel collisionless shock: Cluster observations. *The Astrophysical Journal*, *808*(1), 2. https://doi.org/10.1088/0004-637x/808/1/2

Xu, S., Liemohn, M. W., Dong, C., Mitchell, D. L., Bougher, S. W., & Ma, Y. (2016). Pressure and ion composition boundaries at Mars. *Journal of Geophysical Research: Space Physics*, *121*(7), 6417–6429. https://doi.org/10.1002/2016ja022644

Yang, Z., Jarvinen, R., Guo, X., Sun, T., Koutroumpa, D., Parks, G. K., et al. (2024). Deformations at Earth's dayside magnetopause during quasi-radial IMF conditions: Global kinetic simulations and soft X-ray imaging. *Earth and Planetary Physics*, *8*(1), 59–69. https://doi.org/10.26464/epp2023059

Yang, Z., Lembège, B., & Lu, Q. (2012). Impact of the rippling of a perpendicular shock front on ion dynamics. *Journal of Geophysical Research*, *117*(A7). https://doi.org/10.1029/2011ja017211

Yang, Z., Lu, Q., Lembège, B., & Wang, S. (2009). Shock front nonstationarity and ion acceleration in supercritical perpendicular shocks. *Journal of Geophysical Research*, *114*(A3). https://doi.org/10.1029/2008ja013785

Yi, Y., Zhou, M., Lin, Y., Pang, Y., Jin, R., Song, L., & Deng, X. (2025). Global hybrid simulation of dayside magnetopause energy transport under purely southward interplanetary magnetic field. *Journal of Geophysical Research: Space Physics*, *130*(1), e2024JA033045. https://doi.org/10.1029/2024ja033045

Zhang, H., Sibeck, D., Zong, Q. G., Omidi, N., Turner, D., & Clausen, L. (2013). Spontaneous hot flow anomalies at quasi-parallel shocks: 1. Observations. *Journal of Geophysical Research: Space Physics*, *118*(6), 3357–3363. https://doi.org/10.1002/jgra.50376

Zhang, H., Zong, Q., Connor, H., Delamere, P., Facsko, G., Han, D., et al. (2022). Dayside transient phenomena and their impact on the magnetosphere and ionosphere. *Space Science Reviews*, *218*(5), 40. https://doi.org/10.1007/s11214-021-00865-0

Zhou, Y., Raptis, S., Wang, S., Shen, C., Ren, N., & Ma, L. (2024). Magnetosheath jets at Jupiter and across the solar system. *Nature Communications*, *15*(1), 4. https://doi.org/10.1038/s41467-023-43942-4

Zhou, Y., Shen, C., & Ji, Y. (2023). Undulated shock surface formed after a shock–discontinuity interaction. *Geophysical Research Letters*, *50*(10), e2023GL103848. https://doi.org/10.1029/2023gl103848

Zhou, Y., Wang, B., Raptis, S., Wang, S., Guo, J., Shue, J. H., et al. (2026). Reconstructing the geometry of a hot flow anomaly with bounding jets in magnetosheath. *Geophysical Research Letters*, *53*(3), e2025GL119404. https://doi.org/10.1029/2025gl119404